Article:
Li, Han, Zhang, Xinyu, Halliwell, Tyler et al. (2025) A multi-layer transcranial focused ultrasound model for neuromodulation procedure planning and insertion loss estimation. Physics in Medicine and Biology. 215024. ISSN: 0031-9155

https://doi.org/10.1088/1361-6560/ae1543

Physics in Medicine & Biology

IPEM Institute of Physics and Engineering in Medicine

PAPER • **OPEN ACCESS**

A multi-layer transcranial focused ultrasound model for neuromodulation procedure planning and insertion loss estimation

To cite this article: Han Li *et al* 2025 *Phys. Med. Biol.* **70** 215024

IOP Publishing Phys. Med. Biol. 70 (2025) 215024 https://doi.org/10.1088/1361-6560/ae1543

Physics in Medicine & Biology

IPEM Institute of Physics and Engineering in Medicine

Check for updates

PAPER

A multi-layer transcranial focused ultrasound model for neuromodulation procedure planning and insertion loss estimation

Han Li[1,2,*], Xinyu Zhang[3], Tyler Halliwell[2], Ning Wang[1] and Zhihong Huang[1]

[1] School of Physics, Engineering and Technology, University of York, York YO10 5DD, United Kingdom
[2] School of Science and Engineering, University of Dundee, Dundee DD1 4HN, United Kingdom
[3] School of Medicine, University of Dundee, Dundee DD1 9SY, United Kingdom
[*] Author to whom any correspondence should be addressed.

E-mail: lvw526@york.ac.uk

Keywords: transcranial focused ultrasound, neuromodulation, insertion loss, k-Wave simulation, analytical model

Supplementary material for this article is available online

OPEN ACCESS

RECEIVED
5 July 2025

REVISED
30 September 2025

ACCEPTED FOR PUBLICATION
20 October 2025

PUBLISHED
30 October 2025

Abstract

Objective. Transcranial focused ultrasound (tFUS) for neuromodulation has attracted increasing attention, yet accurate pre-procedural planning and dose estimation is constrained by oversimplified skull representations and by the neglect of transducer-skull spacing induced wave interactions. This study aims to develop and validate a computationally efficient, CT-informed analytical framework for predicting frequency-dependent insertion loss. *Approach.* We propose a multi-layer analytical framework that incorporates four key factors—skull thickness, skull density ratio, ultrasound insertion angle, and the transducer physical geometry and spacing from the skull, to predict frequency-dependent pressure insertion loss. Model accuracy was evaluated against k-Wave simulations and hydrophone measurements in 20 *ex-vivo* human skulls across 100 kHz to 1000 kHz frequency range. *Main Results.* Median prediction deviations for peak pressure insertion loss were +1.1 dB (interquartile range (IQR): +0.2 dB to +2.2 dB) relative to measurement and −1.7 dB (IQR: −2.7 dB to −0.7 dB) relative to simulation. The relative median percentage errors were +30.1% (IQR: +9.5% to +35.6%) and −20.3% (IQR: −31.7% to −10.1%), respectively. Median spearman correlation and cosine similarity values reached 0.92 (IQR: 0.86–0.98, $p < 0.001$) and 0.73 (IQR: 0.49–0.82), respectively. Uncertainty analysis showed that varying transducer-skull spacing resulted in a median absolute percentage uncertainty of 18.1% (IQR: 17.2% to 21.3%). *Significance.* The balance of accuracy and efficiency of the proposed CT-informed multi-layer model makes it a practical tool for transducer positioning, frequency selection, and dose control in tFUS neuromodulation, with potential to improve reproducibility and safety in clinical applications.

1. Introduction

Transcranial focused ultrasound (tFUS) has recently emerged as a promising modality for neuromodulation studies (Legon *et al* 2014, Butler *et al* 2022, Yaakub *et al* 2023, Bancel *et al* 2024, Kosnoff *et al* 2024), offering noninvasive and spatially precise stimulation. Furthermore, it is one of the only non-invasive neuromodulation techniques which can reach deep brain structures. The proposed mechanisms include temporary mechanical disruption of the permittivity of mechano-sensitive ion channels (Kubanek *et al* 2018, Yoo *et al* 2022). *In-vivo* animal studies indicate that the excitement rate of neuronal response depends strongly on the level of local sonication pressure at corresponding ultrasound frequency, typically in the order of hundreds of kilopascals (King *et al* 2013, Kubanek 2018), delivered in milliseconds long bursts. Adverse neuronal inhibitory action may stem from overdosing energy or prolonged sonication (Baek *et al* 2017, Niu *et al* 2022), potentially driven by inertial cavitation or rapid

temperature rise. The risk of such effects increases when exposure exceeds established safety thresholds, such as a mechanical index of 1.9 or a spatial-peak, pulse-average intensity of 190 W cm^{-2} (Pasquinelli *et al* 2019, Murphy *et al* 2025, Aubry *et al* n.d.). Therefore, careful estimation of intracranial pressure remains essential for reducing variability in physiological effects that might otherwise lead to 'reproducibility crisis'(Héroux *et al* 2017).

The skull is the major obstacle to reliable dose modeling, which can substantially attenuate and distort ultrasound signals through reflection, absorption, and scattering (Fry and Barger 1978, White *et al* 1978, 2006a, Pichardo *et al* 2011, Pinton *et al* 2012). In response, many studies employ simulation solvers such as the k-Wave pseudo-spectral time-domain model (Treeby and Cox 2010), which aim to capture full-wave interactions within complex skull morphology. Still, these simulations can be computationally intensive for a full-cranial scale evaluation and rely on broad assumptions about bone properties (Mueller *et al* 2017, Robertson *et al* 2017, McDannold *et al* 2019, Aubry *et al* 2022, Murphy *et al* 2025).

Ray tracing based analytical solutions such as Kranion (Focused Ultrasound Foundation n.d.), Exablate (ExAblate Neuro n.d.), and in-house developed algorithms (Clement and Hynynen 2002, Lu *et al* 2022), designated for helmet-shaped array system to synchronize the arrival phase angle, returning local ray intersected skull thickness, skull density ratio (SDR) and ultrasound insertion angle. Their accuracy at the intended therapeutic frequency has been validated through hydrophone measurement (Jin *et al* 2020) and k-Wave simulation (Bancel *et al* 2021). Nevertheless, several limitations remain such as a uniform bone properties assumption for ray refraction calculations and drops the internal reflections. In such cases, the uncertainty in the estimation of acoustic energy transmission efficiency arises. This is particularly true for sonication pulse length when extended to above dozens of cycles, where wave interference can be pronounced (Krokhmal *et al* 2025, Li *et al* 2025).

Because tFUS neuromodulation currently operates at diagnostic energy level (Baek *et al* 2017) and thus lacks the thermal feedback available in high-intensity ablation, pre-procedural planning should capture these interference phenomena at the working frequency, which is typically across sub-MHz bandwidth (Zhang *et al* 2021). A previous study developed a single skull layer analytical model mapped continuous-sonication insertion loss across the skull surface (Attali *et al* 2023), demonstrating conceptual feasibility but lacking *in-vivo* or *ex-vivo* validation. However, few studies consider the physical presence of the transducer, which could lose the wave-superposition effect also occurring at the transducer-skull spacing (Li *et al* 2025).

To further facilitate the analytical solution for transcranial ultrasound neuromodulation applications, we propose a CT-informed analytical framework that captures several critical determinants of transcranial ultrasound transmission that have been described in previous ray-tracing solutions, that is the skull thickness, SDR, ultrasound insertion angle (Jin *et al* 2020, Focused Ultrasound Foundation n.d.), and layered-bone morphology (Fry and Barger 1978, Hayner and Hynynen 2001). A dynamic segmentation method extracts layer boundaries from CT density profiles, assigning acoustic properties from empirical measurements. The physical transducer surface geometry and its spacing to the skull are modeled so that wave interactions in the water gap are preserved.

We validate the approach by predicting insertion loss in 20 *ex-vivo* human skull samples across 100–1000 kHz frequencies and comparing results with k-Wave simulations and hydrophone measurements. Additional analyses quantify the oscillatory patterns of wave interferences and the sensitivity of insertion loss to transducer-skull spacing. Our aim is to provide a resource-efficient yet accurate tool for tFUS procedure planning, transducer placement and reliable dose estimation.

2. Methods

2.1. *Ex-vivo* human skull samples and CT imaging

Twenty-one *ex-vivo* historical skulls (19 calvaria and 1 half skull for testing, 1 hemi-sected skull for representation) from the Centre for Anatomy and Human Identification, University of Dundee, were scanned in the hydrated condition using Computed Tomography (CT; Revolution EVO, GE, US) with a voxel size of 0.44 × 0.44 × 0.62 mm^3, employing a BonePlus convolution kernel at 120 kVp for enhanced bone delineation. The CT scanned skull volume (figure 1(a)) was transferred to the surface seeds (figure 1(b)) using direct ray-tracing (Attali *et al* 2023). Each seed was mapped to an approximate path to a target region in the thalamus (Li *et al* 2024b). Skull thickness and SDR (Tsai *et al* 2021) was computed along each path. For each seed, the local outer and inner surface angle were estimated by fitting a 5 mm × 5 mm plane around the seed and measuring the normal vector. The average difference between these two vectors and the insertion line defined the local ultrasound insertion angle (figure 1(c)).

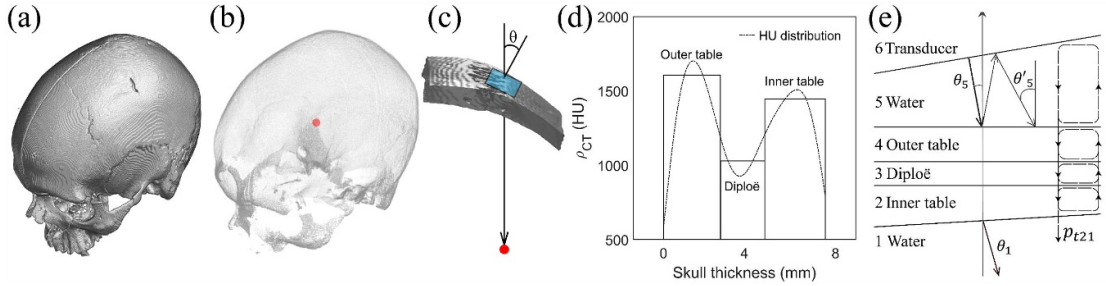

Figure 1. (a) A representative CT skull volume. (b) Skull surface seeds map. Red dot represents an approximated brain target at thalamic region. (c) A representative ultrasound insertion line from the seed to the brain target. Blue shade represents the fitted flat outer surface and its angulation relative to the insertion line. Inner surface angulation was not presented but also considered. (d) Spline represents the HU distribution along the intersected skull thickness. The bars represent the segmented layers thickness and its assigned HU value. (e) Wave propagation scheme of the analytical model, arrows represent the direction of the propagation. p_{t21} represents the exit wave vector, the calculation can be found in appendix.

2.2. Multi-layer analytical structure

Following classic multi-layer approach based on the monochromatic continuous plane wave propagation, (Fry and Barger 1978, Brekhovskikh and Godin 1990, Folds and Loggins n.d.), we empirically defined each seed-to-target intersected skull thickness as a three-layer structure by first leveraging the increasing density from the outer and inner surface (>500 Hounsfield Unit, HU) to the first and second peak density values, respectively, and thresholding the outer and inner table boundary to above approximately 70% and 80% of their peak value. The middle diploe layer situated between the outer and inner table layer. The densities in each layer were averaged to represent the layer bulk density (figure 1(d)). We then added water to the front of the skull and the downstream intracranial domain, given a sub-total of five-layer. This model was subsequently used for a full-scale transmission efficiency analysis prior to incorporating transducer allocation.

We then assumed a concave-shaped transducer (Diameter, $D = 60$ mm, Radius of Curvature, RoC $= 75$ mm, speed of sound, $v = 4300$ m s^{-1} and density, $\rho = 7800$ kg m^{-3}) pointing to the brain target (figure 3(c)), with the transducer surface discretized into 100 5 mm $\times$ 5 mm elements. The angulation vector of each element relative to the outer table surface was computed the same as previous described. The encompassed skull HU was averaged at each layer, resulting in a six-layer total structure (figure 1(e)).

2.3. Analytical solution to predict transcranial insertion loss

Using plane-wave assumptions, we modeled reflections and transmissions at each interface with boundary conditions determined by acoustic impedance (here the mediums were assumed to be semi-infinite). As shown in (figure 1(e)), wave with a unit level of pressure is emitted from the transducer surface and progresses towards the outer table surface. The angulation between the two adjacent surfaces is determined by:

$$\theta = \operatorname{acos}\left(\frac{\overrightarrow{Li} * \overrightarrow{Lj}}{\left|\overrightarrow{Li}\right| * \left|\overrightarrow{Lj}\right|}\right) \tag{1}$$

where $\overrightarrow{Li}$ and $\overrightarrow{Lj}$ represent the vector function of the boundaries i and j.

Upon the initial incidence on the boundary at an angle θ_5, the horizontal propagation component was dropped to only consider the longitudinal mode, thus the wave propagation equation in the spatial domain can be simplified to the following form:

$$p_{i54} = e^{i\varphi_5},\ \varphi_i = k_i z_i cos\theta_i,\ k_i = \frac{w}{c_i} \tag{2}$$

where p_{i54} is the original wave incident upon boundary 54, φ_i denotes to the distance z_i dependent phase advance, k_i is the wavenumber, w is the angular frequency and c_i is the phase velocity.

The total inserted wave p_{t54}, after considering the portion that was directed back to the transducer surface and reflected towards the outer table again, consequently combines with the initial wave to form a superimposed wave, which can be written as:

$$p_{t54} = W_{54} e^{i\varphi_5} \sum_{n=0}^{N} \left(V_{54} V_{56} e^{2i\varphi'_5}\right)^n \tag{3}$$

where V_{ij} and W_{ij} are the reflection and transmission coefficient of the boundary ij. Although a horizontal-infinite assumption was made where wave travels between two boundaries until it vanishes, in practice, the reflected energy decays significantly after two cycles. In an effort to reduce computing load, we set N equals to 2.

For wave emitted from fluid and impinging onto the elastic boundary, that is from water to the bone and transducer, the coefficients of longitudinal waves are Brekhovskikh and Godin (1990):

$$V_{ij} = \frac{Z_j \cos^2 2\theta_{js} + Z_s \sin^2 2\theta_{js} - Z_i}{Z_j \cos^2 2\theta_{js} + Z_s \sin^2 2\theta_{js} + Z_i} \tag{4}$$

$$W_{ij} = \left(\frac{\rho_i}{\rho_j}\right) \frac{2Z_j \cos 2\theta_{js}}{Z_j \cos^2 2\theta_{js} + Z_s \sin^2 2\theta_{js} + Z_i} \tag{5}$$

$$Z_i = \frac{\rho_i c_i}{\cos(\theta_i)},\ Z_j = \frac{\rho_j c_j}{\cos(\theta_j)},\ Z_s = \frac{\rho_j c_{js}}{\cos(\theta_{js})},\quad i = 5, j = 4, 6 \tag{6}$$

where Z_i is the normal impedance of the medium, ρ_i is the density, θ_i is the normal angle of the wave in the layer, and θ_j and θ_{js} are the refracted angle of the longitudinal compression and shear (c_s) wave, and can be determined using Snells law:

$$\frac{\sin\theta_i}{c_i} = \frac{\sin\theta_j}{c_j} = \frac{\sin\theta_{js}}{c_{js}}. \tag{7}$$

The density is derived from CT HU value, using hounsfield2density function (Schneider *et al* 1996, k-Wave MATLAB Toolbox n.d.) provided in k-Wave toolbox. While the speed of sound in bone can vary significantly in different sample conditions (Marsac *et al* 2017), which may introduce bias if directly employing data from other studies, we examined the longitudinal speed of sound from 83 locations (Li *et al* 2025) selected from the smooth surfaces on the utilized calvaria. We performed a simple ultrasound transmit time-of-flight measurement (White *et al* 2006a), with a 1000 kHz plane transducer (Precision acoustics, UK, $D = 23$ mm) arranged from the outer table, and measured with a 1 mm needle hydrophone (Precision acoustics, UK) placed 80 mm away. Our data reveals a linear relationship between CT-derived bulk density and sound speed (figure 2(a)):

$$v = 0.70\rho_{CT} + 1730 \pm 110,\quad R^2 = 0.69 \tag{8}$$

Such longitudinal speed was used to derive the shear speed by multiplying it by a factor of 0.53 (White *et al* 2006a).

The total penetrated wave undergoes another series of propagations in the outer table layer and leaves from boundary 43, waves which exit to the top water layer 5, reflected at boundary 56 and penetrated through 54 are not accounted as the magnitude of this portion of pressure is considered negligible. Therefore, the calculation of transmission through boundary 43 is carried out using the same equation. While in the calculation of the total transmission through layer 32, it is imperative to consider the portion of wave that is reflected at boundary 32, subsequently back propagated through boundary 34, reflected off at boundary 45, transmitted through boundary 43, and finally re-incident upon boundary 32. To determine the total transmission through boundary 32, the equations are expressed as the sum of the original wave p_{t32_orig} and the reflected wave p'_{t32} from boundary 45.

$$p_{t43_{orig}} = p_{t54} W_{43} e^{i\varphi_4} a_4 \sum_{n=0}^{N} \left(V_{43} V_{45} e^{2i\varphi_4} {a_4}^2\right)^n \tag{9}$$

$$p_{t32_{orig}} = p_{t43_{orig}} W_{32} e^{i\varphi_3} a_3 \sum_{n=0}^{N} \left(V_{32} V_{34} e^{2i\varphi_3} {a_3}^2\right)^n \tag{10}$$

$$p_{r34} = p_{t43_{orig}} V_{32} W_{34} e^{2i\varphi_3} {a_3}^2 \sum_{n=0}^{N} \left(V_{32} V_{34} e^{2i\varphi_3} {a_3}^2\right)^n \tag{11}$$

$$p_{r45} = p_{r34} V_{45} W_{43} e^{2i\varphi_4} {a_4}^2 \sum_{n=0}^{N} \left(V_{43} e^{2i\varphi_4} {a_4}^2\right)^n \tag{12}$$

$$p'_{t43} = \frac{p_{r45} p_{t43_{orig}}}{p_{t54}} \tag{13}$$

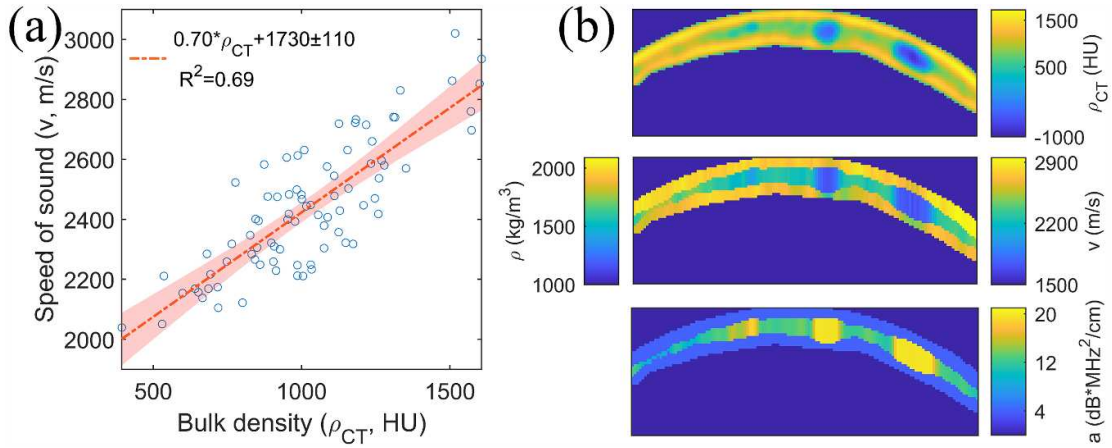

Figure 2. (a) Linear correlation between CT skull bulk density and sound speed. (b) From top to bottom: a representative cross-sectional CT image of a 60 mm × 60 mm skull ROI; reconstructed three-layer skull density and sound speed, and attenuation coefficient maps.

$$p'_{t32} = \frac{p'_{t43} p_{t32_{\text{orig}}}}{p_{t43}} \tag{14}$$

$$p_{t32} = p_{t32_{\text{orig}}} + p'_{t32} \ . \tag{15}$$

The magnitude of the acoustic attenuation of skull has worked out from previous empirical measurement (Li *et al* 2025). We assumed an attenuation coefficient of absorption along the bone thickness a_{TH}, and added a dynamic factor based on the HU contrast ratio between diploe and cortical table a_{SDR} to represent the energy loss due to scattering through heterogeneous structures:

$$a_{\text{TH}} = 4 \cdot F^2 \cdot \left(\text{dBcm}^{-1}\right), a_{\text{TH}} \in [a_4, a_3, a_2] \tag{16}$$

$$a_{\text{SDR}} = 17\,(1 - \text{SDR}) \cdot F^2 \left(\text{dBcm}^{-1}\right), a_{\text{SDR}} \in [a_3] \tag{17}$$

where is the frequency per 1000 kHz and only thought to be valid under 1000 kHz, and a_4, a_3, a_2 represent the attenuated coefficient in outer table, diploe and inner table, respectively.

In the same manner. The total transmission at the boundary 21 can be written as the sum of the original wave p_{t21_orig} and the reflected waves p'_{t21} and p''_{t21} from boundary 34 and 45, respectively.

$$p_{t21} = p_{t21_{orig}} + p'_{t21} + p''_{t21} \ . \tag{18}$$

The corresponding mathematical formulas to calculate transmission and reflection coefficient at skull-water and skull layers interfaces are shown in detail in appendix. We selected one region from each skull model and repeated these calculations across frequencies from 100 kHz to 1000 kHz with 10 kHz steps, and for transducer-skull spacings from 10 mm to 20 mm in the increment of 0.1 mm to form a various degrees of wave super-position. The total computation cost for the analytical sweep at one ROI was completed within seconds on an i7-12700K CPU.

2.4. K-Wave simulation validation

In comparison to the analytical model, we implemented parallel setup in k-Wave. We constructed a 3D grid with voxel size of 0.44 mm, resulting in a 144 × 144 × 196 domain. The selected skull regions (60 mm × 60 mm surface area) were inserted into the simulation, along with one voxel layer of concave piezo-ceramic material (D = 60 mm, RoC = 75 mm, v = 4300 m s^{-1} and ρ = 7800 kg m^{-3}) to where the acoustic source was located (Li *et al* 2024a), mimicking the physical presence of the transducer surface. The physical setup of the skull layer is represented in figure 2(b). The simulation ran on a fluid solver, 18 points per wavelength were calculated, the Boundary Layer Ingestion tolerance was set to 0.9, and the Courant–Friedrichs–Lewy number was set as 0.15 per MHz. Such settings produce stable simulation when incorporated with the piezo layer and with reasonable simulating time consumption. The peak pressure at the focal volume in both free-field and with ROI was recorded. We ran five repeats at

each frequency step and shifted the skull one voxel distance away from the transducer each time to capture wave interference changes. This produced a total of 455 simulations and required 46 h to complete by using Nvidia RTX 3090Ti GPU.

2.5. Hydrophone measurement validation

We next performed underwater hydrophone measurement using two single-element, concave focused transducers (Precision Acoustics, UK) with $D = 60$ mm, RoC $= 75$ mm. Their center frequency is 220 kHz and 680 kHz, and were swept from 100 kHz to 290 kHz and 300 kHz to 1000 kHz, respectively, in 10 kHz increments. We delivered 100 and 150 cycles sinusoidal burst (33500B function generator, Keysight, US; 1020L amplifier, E&I, US), and measured the peak focal pressure with 1 mm needle hydrophone (Precision Acoustics, UK). The power input was tuned to be higher at off-harmonic frequency to compensate for the less efficient resonant response of the transducers, ensuring at least -25 dB and -20 dB coverage in each band, respectively. The captured signal went through the bandpass filter, windowed at the input frequency and with a gate size of 10 Hz. The results were averaged and the produced peak pressure in free field are 0.81 MPa and 1.57 MPa in each sweep bandwidth, respectively.

To measure the transcranial insertion loss, each hydrated, vacuum degassed skull ROI was placed at the pre-defined location, approximately 10 mm away from the transducer aperture (Li *et al* 2025). The same sonication sequence was issued with a total of 10 repeats. After each frequency sweep, the skull was stepped (Velmex, US) 0.4 mm to 0.2 mm away from transducer to sample wave interference effects.

2.6. Statistical analysis

For each skull ROI, we derived three pressure insertion loss curves: analytical model (ANA), k-Wave simulation (SIM), and hydrophone measurement (MEA). Statistical analysis was performed in SPSS V26.0 and Matlab. Frequency-dependent pressure loss level deviations between each pair of curves were computed, along with percentage errors (ε):

$$\varepsilon\left(x,\mathrm{MEA}\right)=\frac{p_x-p_{\mathrm{MEA}}}{p_{\mathrm{MEA}}}*100\%,\quad x\in[\mathrm{ANA},\mathrm{SIM}]$$

$$\varepsilon\left(\mathrm{ANA},\mathrm{SIM}\right)=\frac{p_{\mathrm{ANA}}-p_{\mathrm{SIM}}}{p_{\mathrm{SIM}}}*100\%$$

where p is the normalized intracranial peak pressure. The pressure loss level uncertainty (u) at each frequency was estimated as the average relative deviation of the maximum and minimum values from the mean, expressed as a percentage:

$$u_i=\frac{|p_{i,\max}-\overline{p_i}|+|p_{i,\min}-\overline{p_i}|}{2\overline{p_i}}*100\%.$$

Monotonic agreement was assessed with Spearman correlation (r_s):

$$r_s=1-\frac{6\sum d_i^2}{n\left(n^2-1\right)}$$

where n is the number of paired frequencies ($n = 91$), and d is the difference between the ranks of the paired data with significance threshold of $p < 0.05$. Oscillatory similarity was evaluated by computing the cosine similarity (CS) between the slope vectors of each two paired curves:

$$\mathrm{CS}=\frac{\sum_{i=1}^{n}A_i\cdot B_i}{\sqrt{\sum_{i=1}^{n}A_i^2}\cdot\sqrt{\sum_{i=1}^{n}B_i^2}}$$

where A, B are vectors of the two test results, is the number of frequencies ($n = 91$), and CS represents the CS. Depending on the outcome of the normality test, results are reported as mean $\pm$ standard deviation, or as median values with interquartile range (IQR).

3. Results

3.1. Skull property map and ultrasound transmission efficiency estimation

A total of 553 579 seeds were evenly distributed on the representative skull model, and the seed-to-target ray intersected skull information was remapped to the skull surface, producing high resolution thickness,

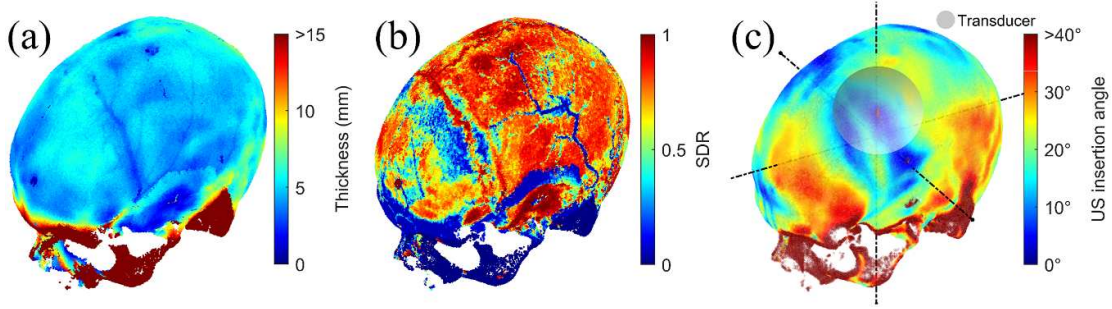

Figure 3. (a), (b) Skull thickness and SDR map. (c) Ultrasound insertion angle relative to the brain target. The transducer was allocated at minimal angulation and adequate distance. Full view animations are provided in supplementary materials.

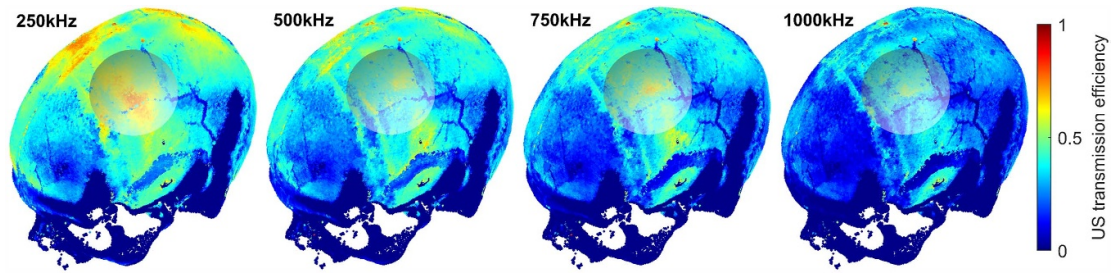

Figure 4. Ultrasound pressure transmission efficiency across the skull surface at four typical frequencies. Transducer layer was not taken into account. Full view animations are provided in supplementary materials.

SDR and insertion angle maps (figure 3). Based on the five-layer structure solution, the estimated ultrasound pressure transmission efficiency at 4 typical frequencies were calculated (figure 4). This information helped determine where the minimal insertion angle and pressure loss were for transducer placement. The corresponding 20 examined skull samples data and the transducer arrangement are shown in appendix, the full volumetric animations of the representative skull model are shown in supplementary materials. The average oblique ultrasound incidence angle over the incident area across 20 ROIs is $9.0 \pm 1.5°$.

3.2. Insertion loss prediction

The skull samples varied widely in physical properties. The 20 ROIs have average thickness of 6.4 ± 1.8 mm, SDR of 0.53 ± 0.19 and CT bulk density of 958 ± 212 HU. Figure 5 compares predicted and measured pressure insertion loss curves over 100–1000 kHz. The generalized linear mixed-model fits for insertion loss (IL, dB) are (figure 6(a)):

$$IL_{\mathrm{MEA}} = -13.9F - 3.5, \quad R^2 = 0.69$$

$$IL_{\mathrm{ANA}} = -14.8F - 1.0, \quad R^2 = 0.73$$

$$IL_{\mathrm{SIM}} = -10.9F - 1.3, \quad R^2 = 0.75$$

Although empirically calibrated attenuation coefficients and sound-speed relations were employed, several trending outliers (e.g. figures 5 and S18) were reproduced by either the analytical model or the k-Wave simulation.

Overall, as shown in figure 6, the analytical model predicted pressure insertion loss magnitude with close alignment: the median deviation relative to measurement was +1.1 dB (IQR: +0.2 dB to +2.2 dB; figure 6(b)) with a median percentage error of +30.1% (IQR: +9.5% to +35.6%; figure 6(c)). This supports the use of a layered skull representation with dynamic, density-dependent attenuation coefficient, although the systematic bias indicates the presence of unmodeled loss mechanisms.

In a highly heterogeneous skull region (S18, TH =8.6 mm, SDR = 0.2, $\rho_{\mathrm{CT}} = 550$), the analytical model reproduced a substantial prediction error, with percentage error reaching +762.3% compared to

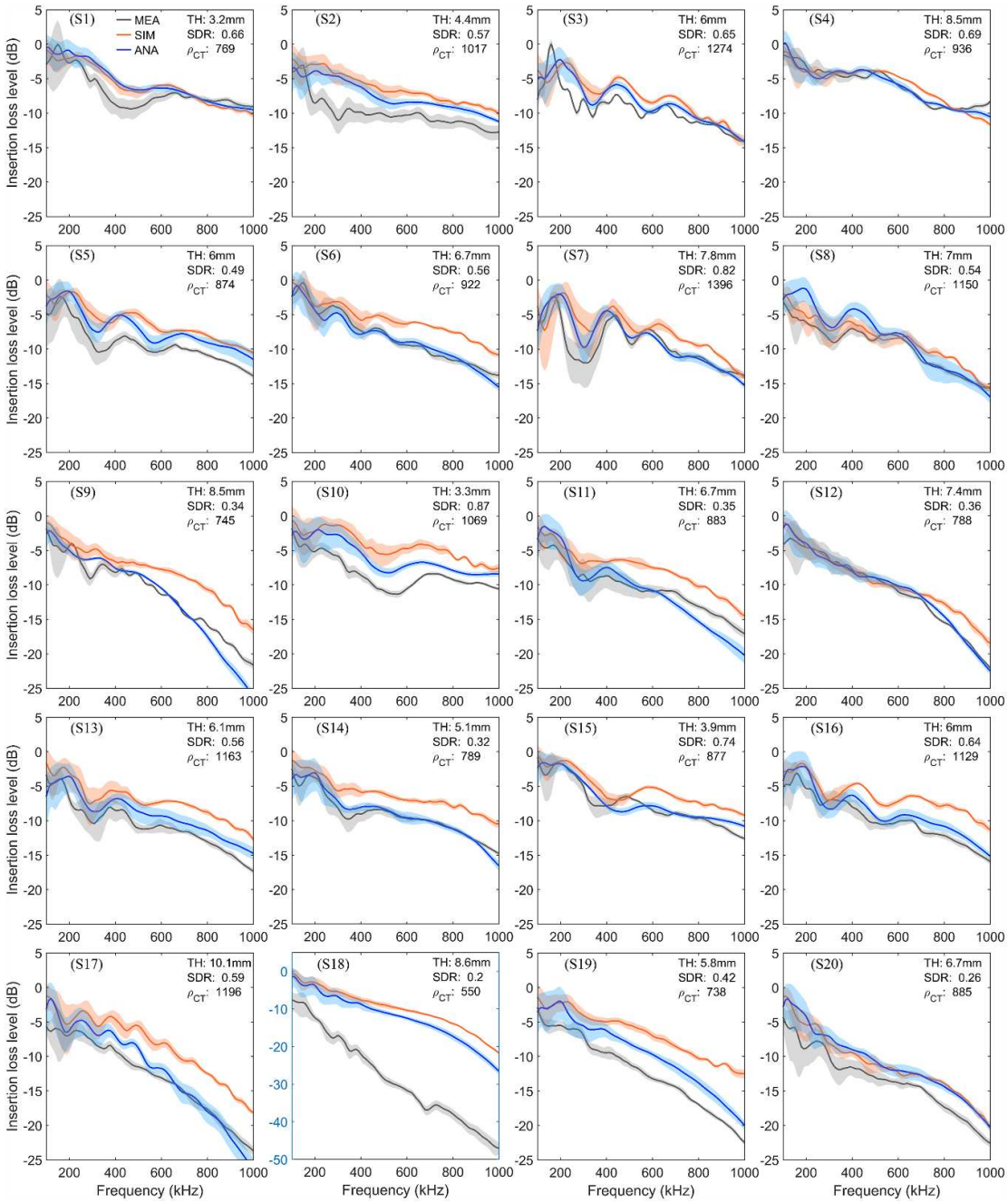

Figure 5. Measured, simulated and analyzed pressure insertion loss levels of 20 skulls' ROI (reported in decibels). The corresponding pressure insertion loss levels in percentage, together with thickness maps, SDR maps and US insertion angle maps are provided in supplement.

measurement (figure 6(c)). By contrast, the remaining 19 ROIs showed percentage error values between −20.5% and +43.3%. Such discrepancies likely reflect local microstructure that is not captured by current three-layer approximation. These findings highlight the importance of refining anisotropic attenuation modeling and integrating more sophisticated segmentation approaches.

The simulation underestimated attenuation, with median deviation of +2.8 dB (IQR: +1.9 dB to +3.6 dB) and median percentage error of +44.0% (IQR: +36.2% to +56.7%), compared to measurement, and +1.7 dB (IQR: +0.7 dB to +2.7 dB) and +20.3% (IQR: +10.1% to +31.7%) to analytical model.

3.3. Influence of transducer-skull spacing

Figure 7(a) illustrates the sensitivity of insertion loss to transducer-skull spacing. At lower frequency (e.g. 150 kHz), shifting the skull by a few millimeters altered measured insertion loss from −5.3 dB to +2.9 dB. This sensitivity diminished with frequency, stabilizing at ±0.6 dB roughly beyond 650 kHz,

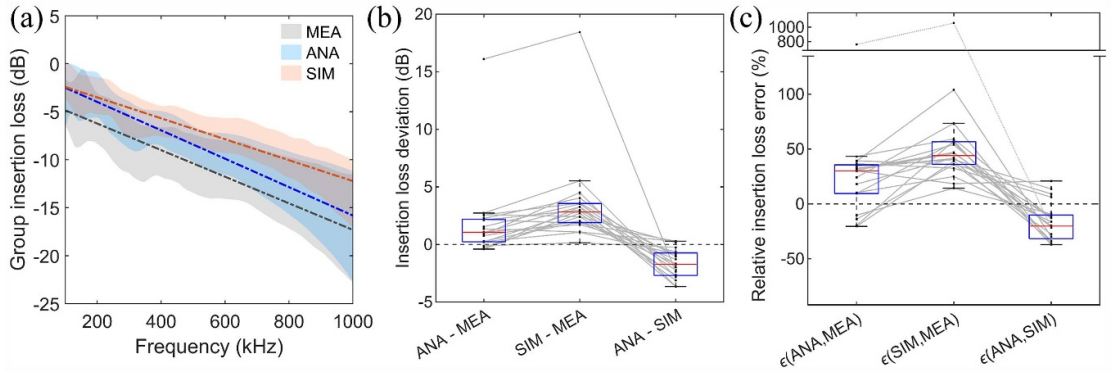

Figure 6. (a) Group insertion loss averaged over 20 skulls' ROI. (b) Inter-group pressure insertion loss deviation between each two results. ANA—MEA: median: +1.1 dB, max: +16.1 dB, min: −0.4 dB; SIM—MEA: median: +2.8 dB, max: +18.4 dB, min: +0.2 dB; ANA—SIM: median: −1.7 dB, max: +0.3 dB, min: −3.7 dB. (c) Inter-group pressure insertion loss error in percentage: ε(ANA,MEA): median: +30.1%, max: +762.3%, min: −20.5%; ε(SIM,MEA): median: +44.0%, max: +1057.0%, min: +14.4%; ε(ANA,SIM): median: −20.3%, max: +20.9%, min: −37.2%.

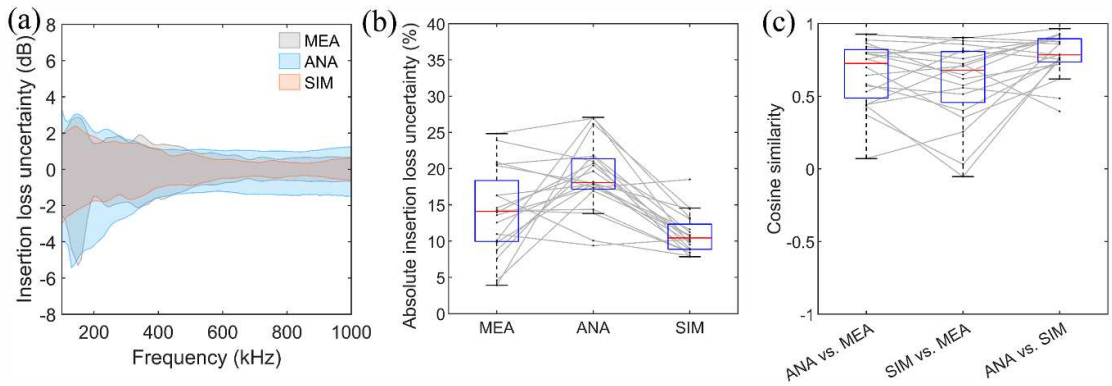

Figure 7. (a) Average insertion loss uncertainties caused by varying transducer-skull spacing over 20 skulls ROI. (b) Absolute insertion loss uncertainty averaged over frequency: MEA: median: 14.1%, max: 24.8%, min: 3.9%; ANA: median: 18.1%, max: 27.1%, min: 9.4%; SIM: median: 10.4%, max: 18.5%, min: 7.9%. (c) Inter-group comparison of cosine similarity of each two result curves. ANA vs. MEA: median: 0.73, max: 0.93, min: 0.07; SIM vs. MEA: median: 0.68, max: 0.91, min: −0.05; ANA vs. MEA: median: 0.79, max: 0.97, min:0.40.

where absorption effects dominate interference. The median pressure loss uncertainty in percentage across 20 ROIs is 14.1%(IQR: 10.0% to 18.4%; figure 7(b)). The simulation reproduced the overall trend but sampled fewer spacing and therefore underestimates the peak uncertainty, with a median uncertainty in percentage of 10.4% (IQR: 8.9% to 12.3%). In contrast, the analytical model, evaluated at 0.1 mm increments, predicted average uncertainties from −2.0 dB to +1.4 dB, marginally higher than the simulation and measurement, and with uncertainty in percentage of 18.1% (IQR: 17.2% to 21.3%). These results demonstrate that the physical presence of transducer affects transmitted energy, particularly at lower frequencies.

3.4. Insertion loss oscillatory behavior

As shown in figure 5, insertion loss shows pronounced oscillation at lower frequencies (approximately < 700 kHz), observed in more than half of the tested ROIs, indicative of constructive and destructive wave interference within skull thickness. Oscillation amplitude depended on multiple morphology factors, such as the thickness variability, RoC, and also appeared to be more severe in ROIs with thin thickness, high bulk density or high SDR.

Analytical predictions reproduced the oscillatory pattern that in general agreement with the measurements (median $r_s = 0.92$, IQR: 0.86–0.98, $p < 0.001$; median CS = 0.73, IQR: 0.49–0.82; figure 7(c)). Simulation exhibited similar but slightly weaker agreement (median $r_s = 0.91$, IQR: 0.86–0.98, $p < 0.001$; median CS = 0.68, IQR: 0.46–0.81). Trending mismatches obviously occurred at S15 and S17 in both predicting methods, suggesting that speed of sound and layers were not accurately represented. Stronger correlation is evident between simulation and analytical results (median $r_s = 0.97$,

IQR: 0.96–0.99, $p < 0.001$; median CS = 0.79, IQR: 0.74–0.90), suggesting that the wave phase modeling captures wave interactions almost as effectively as solving the differential wave-equation.

4. Discussion

This study presents a CT-informed, six-layer analytical model for predicting tFUS pressure insertion loss. Cross-validation against k-Wave simulations and hydrophone measurements in 20 *ex-vivo* skull samples confirms that the framework reproduces key interference phenomena across sub-MHz frequencies while remaining computationally tractable. High correlation among the three techniques underscores the value of layered, acoustic impedance-based approach for rapid insertion loss estimation during tFUS planning. Notwithstanding, this study was conducted using *ex-vivo* skulls, which may not fully capture the diversity of *in-vivo* cranial conditions. Although all *ex-vivo* skulls were rehydrated prior to testing, differences in marrow composition and microstructures may alter acoustic transmission relative to living tissue. In addition, the absence of surrounding tissues, including scalp, dura mater, and brain tissue limits its direct translational applicability. Future work should incorporate more physiologically realistic bone models, such as freshly excised or realistically embalmed skulls to better assess clinical applicability.

One of the most notable findings was the prevalence of constructive and destructive interference patterns, producing oscillatory insertion loss curves in both measurements and predictions. Such interference pattern arises from multiple reflections at the water-transducer interface (Li *et al* 2025), the skull-water interface, and the internal interfaces between skull layers (Aarnio *et al* 2005). Beyond approximately 700 kHz, the oscillation amplitude decreases as absorption governs. Because sub-MHz frequencies are favored for neuromodulation (deeper penetration with minimal heating), recognizing these interference patterns is essential for dose control. In this study, the patterns were observed at short transducer-skull spacings, representing conditions for targeting deeper brain regions such as the thalamus. Superficial cortical targets are also of interest, and prior work showed that qualitative interference patterns remained consistent across both short (10 mm–20 mm) and long (40 mm–50 mm) spacings (Li *et al* 2025), suggesting that oscillatory behavior would also occur when targeting more superficial structures. Although the analytical model was evaluated the spacing effect at fine increments of 0.1 mm, practical considerations limited the simulations to 0.44 mm, as each frequency spectrum sweep required approximately 10 h to complete.

4.1. Comparison with other bone modeling strategies

Several analytical studies used single-layer representations with spatially averaged properties, which recovered fluctuation trends in energy transmission (White *et al* 2006b, Attali *et al* 2023,). Fry and Barger (1978) proposed a three-layer bone model, quantifying phase speed and phase angle in different layers, and reporting a diploe-specific loss coefficient of 11.5 dB/(MHz^4 cm) based on the squared difference of bulk modulus between the blood–bone matrix and blood-fat matrix. Hayner and Hynynen (2001) further expanded the solution to encompass an additional scalp layer and incorporated oblique ultrasound incidence. While these models demonstrated that intracranial pressure maxima occur at skull resonance frequencies, none accounted for the physical presence of the transducer or for wave superposition in the intervening water path.

The present work extends this lineage by introducing the transducer modeling, discretizing the aperture into differential area and allowing wave to interact between transducer-skull spacing. This yields a more comprehensive tFUS transmission domain without incurring the prohibitive run-times of full-wave solvers.

Nevertheless, the three-layer skull representation used here remains a simplification of cranial bone heterogeneity. To partially address spatial variability, we employed a voxel-wise adaptive three-layer model, allowing adjacent rays to traverse distinct local layer thicknesses and property assignments. More adaptive segmentation strategies, such as dynamic multi-layer skull modeling, could in principle improve fidelity in regions with complex anatomy (e.g. the squamosal suture where overlapping bone violates the three-layer assumption, or in diploë containing interdigitating vasculature), however, analytical complexity would increase substantially, and accurate delineation is further constrained by the limited resolution of current clinical CT. This trade-off may explain why most existing skull analytical models have been restricted to three layers, which remain sufficient in many cases. Severe local variations in porosity and microarchitecture, as observed in S18, can nevertheless lead to large discrepancies in insertion loss predications, indicating that strongly anisotropic and heterogeneous cranial bone cannot be faithfully represented by layered decomposition alone. Due to the limited number of specimens, we could not

Table 1. Peak pressure transmission ratio comparison with other studies. Literatures unspecified to cycles of burst, skull thickness and density, or transducer characteristics.

	MEA	ANA	SIM	MEA	ANA	SIM
	Peak pressure transmission ratio					
Frequency	Present study, interquartile range			Literature		
250 kHz	[34% 57%]	[47% 65%]	[57% 76%]	32%, 270 kHz (Gimeno *et al* 2019); 46%, 270 kHz (Krokhmal *et al* 2025)	72%, 200 kHz (Attali *et al* 2023)	49%, 250 kHz (Lee *et al* 2015); 47%, 250 kHz (Hosseini *et al* 2023); 43%, 270 kHz (Lee *et al* 2016)
500 kHz	[28% 38%]	[35% 43%]	[41% 52%]	70%, 500 kHz (Legon *et al* 2018); 50%, 500 kHz (Legon *et al* 2014); 31%, 500 kHz (Krokhmal *et al* 2025)	62%, 500 kHz (Attali *et al* 2023)	65%, 500 kHz (Yaakub *et al* 2023); 29%, 500 kHz (Strohman *et al* 2024); 39%, 500 kHz (Hosseini *et al* 2023)
750 kHz	[17% 31%]	[21% 35%]	[33% 42%]	17%, 750 kHz (Chen *et al* 2023); 21%, 750 kHz (Krokhmal *et al* 2025)	35%, 700 kHz (White *et al* 2006b); 23%, 750 kHz (Hayner and Hynynen 2001); 57%, 800 kHz (Attali *et al* 2023)	31%, 750 kHz (Hosseini *et al* 2023)
1000 kHz	[8% 23%]	[9% 27%]	[16% 30%]	15%, 1000 kHz (Pinton *et al* 2012); 14%, 1000 kHz (Krokhmal *et al* 2025)	53%, 1000 kHz (Attali *et al* 2023); 15%, 1000 kHz (Guo *et al* 2022)	15%, 1000 kHz (Pinton *et al* 2012)

quantify a structural heterogeneity threshold beyond which prediction errors become unacceptable. But it shall be reasonable to assume that thick or highly heterogeneous skulls pose greater challenges.

Two factors may help explain why the simplified three-layer representation remained largely effective in this study. First, the sub-MHz frequency range employed here yield wavelengths several times larger than typical trabecular bone spacing (approximately 0.83 mm in highly porous regions (Chaffaí *et al* 2002)), which reduces but does not eliminate microstructure-induced scattering. Second, the near-normal incidence reduced the likelihood of refraction-driven shear mode conversion. In instances where the three-layer approximation is inadequate, full-wave simulations may provide an alternative; although their accuracy is also constrained by the wide variability in reported correlations between HU and acoustical parameters. Such uncertainty may partly arise from differences in CT acquisition parameters (Aubry *et al* 2003, Montanaro *et al* 2021). In our work, the simulation model tended to underestimated attenuation compared to both measurements and the analytical model. This discrepancy is unlikely to arise from insufficient attenuation coefficient settings alone, a potential cause may instead stem from modeling the domain as purely fluid mediums rather than viscoelastic, although the significance has not yet been verified due to the significant increase in time investment. Despite these challenges, both the analytical and simulation models demonstrated pressure insertion loss predictions that generally trended with hydrophone measurements.

Table 1 compares 25% to 75% IQR of peak transmitted pressure ratio obtained by MEA, ANA and SIM with published values at four typical (or similar) frequencies. Discrepancies across studies

are attributable to variability in skull morphology, transducer geometry and driving waveform. It is worth noting that, because the proposed analytical model generally underestimated pressure insertion loss, compensating for this bias would require increasing the applied pressure to achieve a desired *in situ* value. However, given the variability in prediction errors (−20.5% to +43.3%, with one outlier at +762.3%) and uncertainty from transducer-skull spacing (9.4% to 27.1%), such adjustments risk overshooting guideline safety limits for mechanical index or acoustic intensity in individual cases. Therefore, the analytical model is better interpreted as a relatively conservative predictors, suitable for supporting treatment planning while recognizing that deviations in either direction can still occur. Safe application should also involve verification against maximum allowable safety limits at the corresponding frequency, with adjustments made downward as needed.

The present validation was limited to an upper frequency of 1000 kHz by the bandwidth constraint of the transducers employed. While this range covers the majority of clinical tFUS studies, higher frequencies above 1000 kHz are also used in neuromodulation studies (Di Biase *et al* 2019). Extending validation into this range would enhance translational relevance. Future studies could employ broader-bandwidth transducers to enable reliable testing at these higher frequencies.

The present model emphasizes longitudinal transmission but allows for shear-wave excitation through the use of an elastic-wave formulation. Because the transducer surface was positioned nearly normal to the skull surface, shear contributions were expected to be minimal in the central aperture. At more oblique incidence near the periphery, however, partial conversion into shear mode likely occurs. Although this effect is implicitly included, the model does not explicitly quantify the proportion of energy transmitted through as shear waves, which may lead to higher insertion loss prediction uncertainty at larger incidence angles.

4.2. Transducer allocation

Existing transducer placement methods either minimize surface reflection from the skull surface (Park *et al* 2019), simulating intracranial ultrasound pressure attenuation (Gao *et al* 2023), or by visually inspecting the back-propagated US phase map from the brain target (Butler *et al* 2022). By integrating the ultrasound insertion angle, skull thickness, SDR and transmission efficiency maps, our pipeline produces a full-scale skull evaluation. A complete atlas generation consumed approximately 25 h for a full skull and 6 h for calvaria by using i7-12700K CPU. In comparison, a full-scale k-Wave simulation for a skull at one frequency requires nearly 500 h (Gao *et al* 2023).

5. Conclusion

In summary, the six-layer analytical model proposed here integrates skull thickness and SDR, ultrasound insertion angle, and transducer geometry to yield insertion loss predictions that generally align closely with both simulation and experimental measurements. The median predicted insertion loss deviation was maintained at +1.1 dB (IQR: +0.2 dB to +2.2 dB) and −1.7 dB (IQR: −2.7 dB to −0.7 dB) when compared to the measurement and simulation output, respectively. The relative median error in percentage are +30.1% (IQR: +9.5% to +35.6%) and −20.3% (IQR: −31.7% to −10.1%), respectively. The median percentage uncertainty induced by varying transducer-skull spacing was predicted to be 18.1% (IQR: 17.2% to 21.3%), marginally higher than the simulation and measurement. The three sets of results show moderate to high oscillatory similarity and high trending correlations. Additionally, the required computing time for analytical model is in the matter of hours. This balance of accuracy and computational efficiency positions the model as a valuable tool for tFUS neuromodulation procedure planning—one that can inform transducer placement, predict optimal frequency usage, and reduce the variability in delivered ultrasound energy.

Data availability statement

The data that support the findings of this study are openly available at the following URL/DOI: https://github.com/HanLiUoY/tFUS-model-for-neuromodulation-procedure-planning-and-transmission-efficiency-estimation-.git. Data will be available from 01 May 2026.

Supplementary Material available at https://doi.org/10.1088/1361-6560/ae1543/data1.

Acknowledgment

The experimental work was conducted in University of Dundee, and the author expresses deep appreciation to Dr Tom Gilbertson, Dr Isla Barnard, Professor. Andreas Melzer, and Mr. Alan Webster for technical and academic support.

Conflict of interest

The authors have no conflicts of Interest to disclose.

Ethics approval

Approval of the use of human tissue specimens in the study was given by the University of Dundee Thiel Advisory group. This research complies with the Anatomy Act (1984) and the Human Tissue (Scotland) Act 2006.

Author contributions

Han Li 0009-0002-9937-0548
Conceptualization (lead), Data curation (lead), Formal analysis (lead), Methodology (lead), Writing – original draft (lead)

Xinyu Zhang
Conceptualization (supporting), Formal analysis (lead), Software (lead), Validation (lead), Writing – review & editing (supporting)

Tyler Halliwell 0009-0002-9987-2927
Investigation (lead), Resources (lead), Writing – review & editing (lead)

Ning Wang
Conceptualization (supporting), Software (lead), Visualization (lead), Writing – review & editing (supporting)

Zhihong Huang
Conceptualization (lead), Investigation (lead), Project administration (lead), Resources (lead), Supervision (lead), Writing – review & editing (lead)

Appendix. Transmission and reflection coefficient

Skull-water interface

$$V_{ij} = \frac{Z_j + Z_s \sin^2 2\theta_{is} - Z_i \sin^2 2\theta_{is}}{Z_j + Z_s \sin^2 2\theta_{is} + Z_i \sin^2 2\theta_{is}}$$

$$W_{ij} = \frac{\left(1 - V_{ij}\right) \tan\theta_j \cot\theta_i}{\cos 2\theta_{is}}$$

where

$$Z_i = \frac{\rho_i c_i}{\cos\theta_i},\ Z_s = \frac{\rho_i c_{is}}{\cos\theta_{is}},\ Z_j = \frac{\rho_j c_j}{\cos\theta_j}, \quad i = 2, j = 1.$$

Skull layers interface

$$V_{ij} = \left[\left(b\xi_i - d\xi_j\right) F - \left(a + e\xi_i \eta_j\right) H\zeta^2\right] D^{-1}$$

$$W_{ij} = \left(\frac{Z_j}{Z_i}\right) 2\rho_i \xi_i \left(c_i / c_j\right) \mathrm{FD}^{-1}$$

where

$$a = \gamma_j - \gamma_i,\ \ b = \gamma_j + \chi_i \zeta,\ \ d = \gamma_j + \chi_i \zeta,\ \ e = 2\rho_j {c_{js}}^2 - \rho_i {c_{is}}^2,$$

$$\chi_l = 2\rho_l c_l \zeta,\ \ \gamma_l = \rho_l\left(1 - 2c_l^2\zeta^2\right),\ \ \xi_l = \frac{cos\theta_l}{c_l},\ \ \eta_l = \frac{cos\theta_{ls}}{c_{ls}},$$

$$l = i, j = 2, 3, 4$$

$$E = b\xi_i + d\xi_j,\ \ F = b\eta_i + d\eta_j,\ \ G = a - e\xi_i\eta_j,$$

$$H = a - e\xi_i\eta_j,\ \ D = EF + GH\zeta^2.$$

Skull physical property and ultrasound insertion maps for S1 to S20

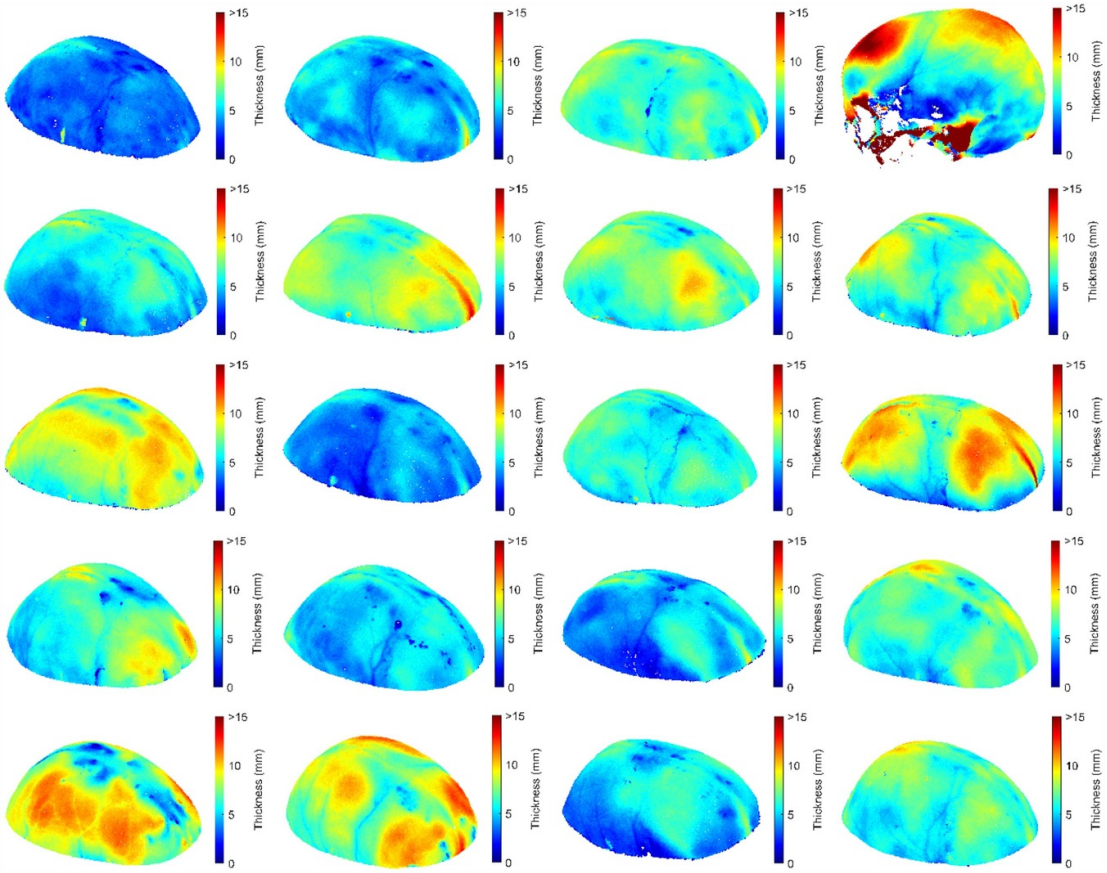

Figure 8. Skull thickness map of S1–S20 in the same order of insertion loss plots to the figure 5 in the paper.

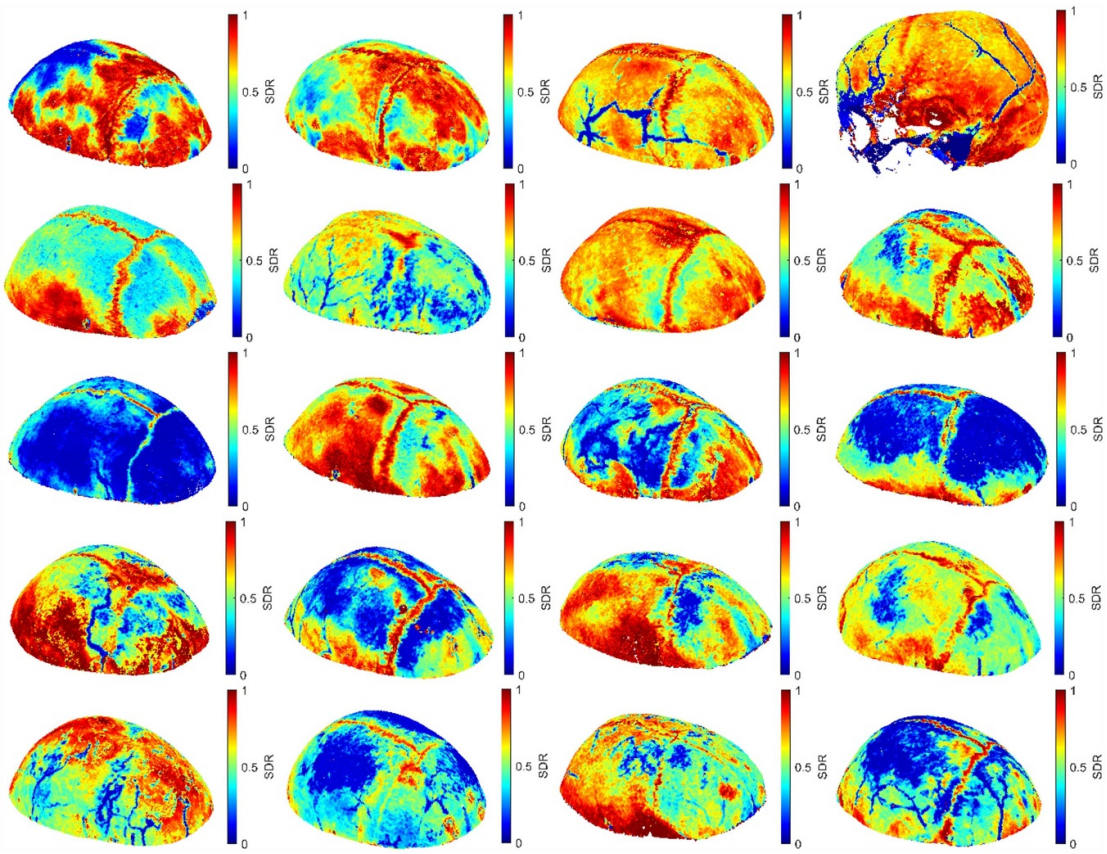

Figure 9. Skull SDR map of S1–S20.

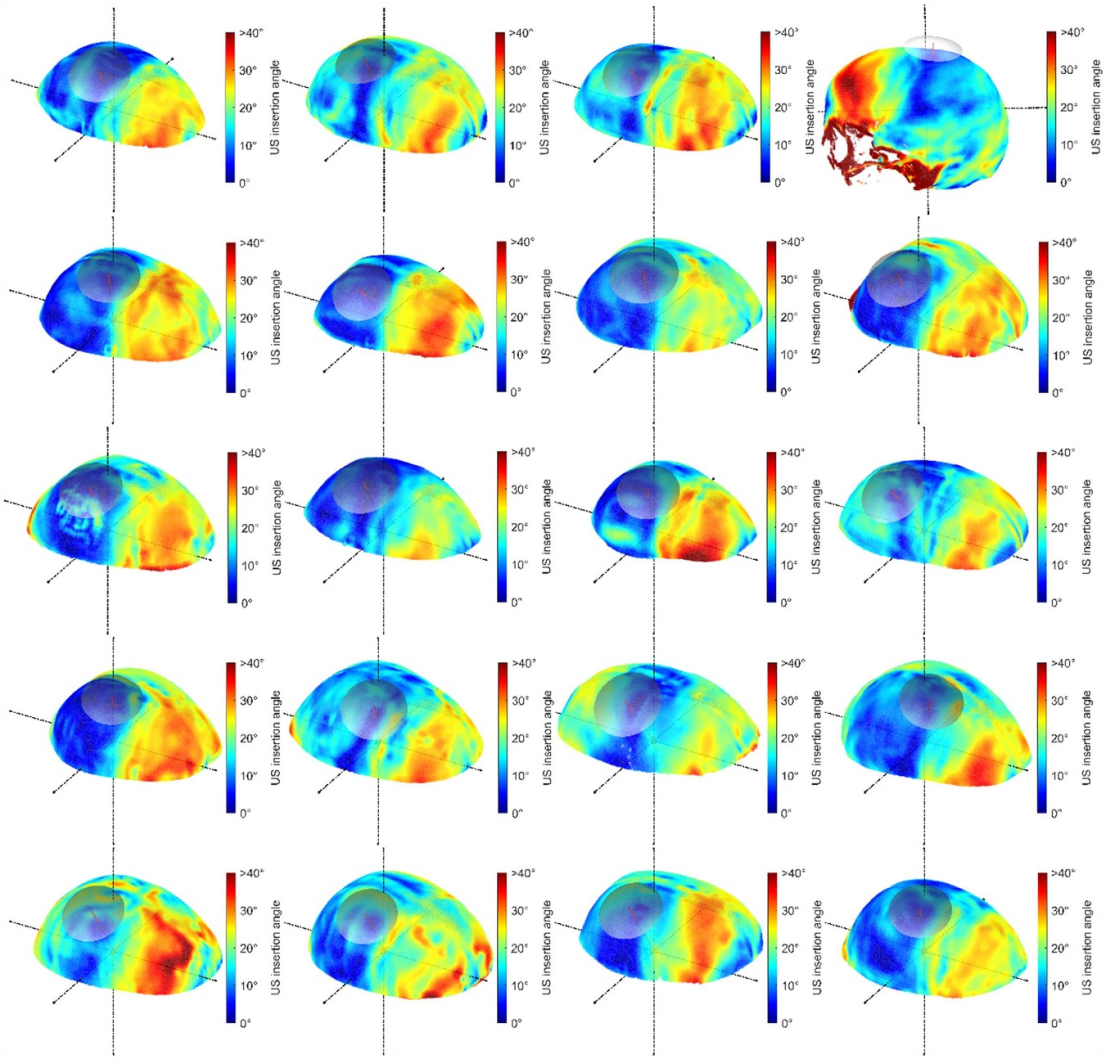

Figure 10. US insertion angle map with transducer placement of S1–S20. This angle is averaged over the inner and outer skull surface angle, and prior to taking ultrasound emission angle into account.

References

Aarnio J, Clement G T and Hynynen K 2005 A new ultrasound method for determining the acoustic phase shifts caused by the skull bone *Ultrasound Med. Biol.* **31** 771–80

Attali D *et al* 2023 Three-layer model with absorption for conservative estimation of the maximum acoustic transmission coefficient through the human skull for transcranial ultrasound stimulation *Brain Stimul.* **16** 48–55

Aubry J-F *et al* 2022 Benchmark problems for transcranial ultrasound simulation: intercomparison of compressional wave models *J. Acoust. Soc. Am.* **152** 1003–19

Aubry J-F *et al* n.d. ITRUSST consensus on biophysical safety for transcranial ultrasonic stimulation

Aubry J-F, Tanter M, Pernot M, Thomas J-L and Fink M 2003 Experimental demonstration of noninvasive transskull adaptive focusing based on prior computed tomography scans *J. Acoust. Soc. Am.* **113** 84–93

Baek H, Pahk K J and Kim H 2017 A review of low-intensity focused ultrasound for neuromodulation *Biomed. Eng. Lett.* **7** 135–42

Bancel T *et al* 2024 Sustained reduction of essential tremor with low-power non-thermal transcranial focused ultrasound stimulations in humans *Brain Stimul.* **17** 636–47

Bancel T, Houdouin A, Annic P, Rachmilevitch I, Shapira Y, Tanter M and Aubry J-F 2021 Comparison between ray-tracing and full-wave simulation for transcranial ultrasound focusing on a clinical system using the transfer matrix formalism *IEEE Trans. Ultrason. Ferroelectr. Freq. Control* **68** 2554–65

Brekhovskikh L M and Godin O A 1990 *Acoustics of Layered Media I* vol 5 (Springer) (https://doi.org/10.1007/978-3-642-52369-4)

Butler C R, Rhodes E, Blackmore J, Cheng X, Peach R L, Veldsman M, Sheerin F and Cleveland R O 2022 Transcranial ultrasound stimulation to human middle temporal complex improves visual motion detection and modulates electrophysiological responses *Brain Stimul.* **15** 1236–45

Chaffaí S, Peyrin F, Nuzzo S, Porcher R, Berger G and Laugier P 2002 Ultrasonic characterization of human cancellous bone using transmission and backscatter measurements: relationships to density and microstructure *Bone* **30** 229–37

Chen M *et al* 2023 Numerical and experimental evaluation of low-intensity transcranial focused ultrasound wave propagation using human skulls for brain neuromodulation *Med. Phys.* **50** 38–49

Clement G T and Hynynen K 2002 Micro-receiver guided transcranial beam steering *IEEE Trans. Ultrason. Ferroelectr. Freq. Control* **49** 447–53
Di Biase L, Falato E and Di Lazzaro V 2019 Transcranial focused ultrasound (tFUS) and transcranial unfocused ultrasound (tUS) neuromodulation: from theoretical principles to stimulation practices *Front. Neurol.* **10** 549
ExAblate Neuro n.d. Exablate 4000 type 1.1 SW 7.2 operator manual CE Rev5.8, insightec, Tirat Carmel, Israel, Jan. 2019.—Google search (available at: www.google.com/search?q=Exablate+4000+Type+1.1+SW+7.2+Operator+Manual+CE+Rev5.8%2C+Insightec%2C+Tirat+Carmel%2C+Israel%2C+Jan.+2019.&rlz=1C1GCEU_zh-CNGB1162GB1162&oq=Exablate+4000+Type+1.1+SW+7.2+Operator+Manual+CE+Rev5.8%2C+Insightec%2C+Tirat+Carmel%2C+Israel%2C+Jan.+2019.&gs_lcrp=EgZjaHJvbWUyBggAEEUYOTIHCAEQIRiPAjIHCAIQIRiPAjIHCAMQIRiPAtIBBzkwNWowajeoAgCwAgA&sourceid=chrome&ie=UTF-8) (Accessed 25 May 2025)
Focused Ultrasound Foundation n.d. Kranion (available at: www.fusfoundation.org/for-researchers-and-clinicians/resources/kranion/) (Accessed 23 May 2025)
Folds D L and Loggins C D n.d. Transmission and reflection of ultrasonic waves in layered media *J. Acoust. Soc. Am.* **62** 1102–9
Fry F J and Barger J E 1978 Acoustical properties of the human skull *J. Acoust. Soc. Am.* **63** 1576–90
Gao P, Sun Y, Zhang G, Li C and Wang L 2023 A transducer positioning method for transcranial focused ultrasound treatment of brain tumors *Front. Neurosci.* **17** 1277906
Gimeno L A, Martin E, Wright O and Treeby B E 2019 Experimental assessment of skull aberration and transmission loss at 270 kHz for focused ultrasound stimulation of the primary visual cortex *IEEE Int. Ultrasonics Symp., IUS* (*October 2019*) pp 556–9
Guo J, Song X, Chen X, Xu M and Ming D 2022 Mathematical model of ultrasound attenuation with skull thickness for transcranial-focused ultrasound *Front. Neurosci.* **15** 778616
Hayner M and Hynynen K 2001 Numerical analysis of ultrasonic transmission and absorption of oblique plane waves through the human skull *J. Acoust. Soc. Am.* **110** 3319–30
Héroux M E, Loo C K, Taylor J L and Gandevia S C 2017 Questionable science and reproducibility in electrical brain stimulation research *PLoS One* **12** e0175635
Hosseini S, Puonti O, Treeby B, Hanson L G and Thielscher A 2023 A head template for computational dose modelling for transcranial focused ultrasound stimulation *Neuroimage* **277** 120227
Jin C, Moore D, Snell J and Paeng D-G 2020 An open-source phase correction toolkit for transcranial focused ultrasound *BMC Biomed. Eng.* **2** 9
k-Wave MATLAB Toolbox n.d. hounsfield_density
King R L, Brown J R, Newsome W T and Pauly K B 2013 Effective parameters for ultrasound-induced *in vivo* neurostimulation *Ultrasound Med. Biol.* **39** 312–31
Kosnoff J, Yu K, Liu C and He B 2024 Transcranial focused ultrasound to V5 enhances human visual motion brain-computer interface by modulating feature-based attention *Nat. Commun.* **15** 1–18
Krokhmal A, Simcock I C, Treeby B E and Martin E 2025 A comparative study of experimental and simulated ultrasound beam propagation through cranial bones *Phys. Med. Biol.* **70** 025007
Kubanek J 2018 Neuromodulation with transcranial focused ultrasound *Neurosurg. Focus* **44** E14
Kubanek J, Shukla P, Das A, Baccus S A and Goodman M B 2018 Ultrasound elicits behavioral responses through mechanical effects on neurons and ion channels in a simple nervous system *J. Neurosci.* **38** 3081–91
Lee W, Kim H C, Jung Y, Chung Y A, Song I U, Lee J H and Yoo S S 2016 Transcranial focused ultrasound stimulation of human primary visual cortex *Sci. Rep.* **6** 34026
Lee W, Kim H, Jung Y, Song I U, Chung Y A and Yoo S S 2015 Image-guided transcranial focused ultrasound stimulates human primary somatosensory cortex *Sci. Rep.* **5** 8743
Legon W, Ai L, Bansal P and Mueller J K 2018 Neuromodulation with single-element transcranial focused ultrasound in human thalamus *Hum. Brain Mapp.* **39** 1995–2006
Legon W, Sato T F, Opitz A, Mueller J, Barbour A, Williams A and Tyler W J 2014 Transcranial focused ultrasound modulates the activity of primary somatosensory cortex in humans *Nat. Neurosci.* **17** 322–9
Li H, Barnard I, Halliwell T, Gilbertson T and Huang Z 2024a Enhancing transcranial focused ultrasound simulation accuracy: the impact of transducer geometry and skull modelling *2024 IEEE Ultrasonics, Ferroelectrics, and Frequency Control Joint Symp. (UFFC-JS)* (IEEE) pp 1–4
Li H, Barnard I, Halliwell T, Zhang X, Melzer A and Huang Z 2025 Effects of skull properties on continuous-wave transcranial focused ultrasound transmission *J. Acoust. Soc. Am.* **157** 2336–49
Li H, Liu X, Zhao Y, Wang Z and Huang Z 2024b Advancing transcranial focused ultrasound for neuromodulation: integration of pseudo-brain model into simulations *2024 IEEE Ultrasonics, Ferroelectrics, and Frequency Control Joint Symp. (UFFC-JS)* (IEEE) pp 1–3
Lu N, Hall T L, Sukovich J R, Choi S W, Snell J, McDannold N and Xu Z 2022 Two-step aberration correction: application to transcranial histotripsy *Phys. Med. Biol.* **67** 125009
Marsac L, Chauvet D, La Greca R, Boch A L, Chaumoitre K, Tanter M and Aubry J-F 2017 Ex vivo optimisation of a heterogeneous speed of sound model of the human skull for non-invasive transcranial focused ultrasound at 1 MHz *Int. J. Hyperth.* **33** 635–45
McDannold N, White P J and Cosgrove R 2019 Elementwise approach for simulating transcranial MRI-guided focused ultrasound thermal ablation *Phys. Rev. Res.* **1** 033205
Montanaro H, Pasquinelli C, Lee H J, Kim H, Siebner H R, Kuster N, Thielscher A and Neufeld E 2021 The impact of CT image parameters and skull heterogeneity modeling on the accuracy of transcranial focused ultrasound simulations *J. Neural Eng.* **18** 046041
Mueller J K, Ai L, Bansal P and Legon W 2017 Numerical evaluation of the skull for human neuromodulation with transcranial focused ultrasound *J. Neural Eng.* **14** 066012
Murphy K R *et al* 2025 A practical guide to transcranial ultrasonic stimulation from the IFCN-endorsed ITRUSST consortium *Clin. Neurophysiol.* **171** 192–226
Niu X, Yu K and He B 2022 Transcranial focused ultrasound induces sustained synaptic plasticity in rat hippocampus *Brain Stimul.* **15** 352–9
Park T Y, Pahk K J and Kim H 2019 Method to optimize the placement of a single-element transducer for transcranial focused ultrasound *Comput. Methods Programs Biomed.* **179** 104982
Pasquinelli C, Hanson L G, Siebner H R, Lee H J and Thielscher A 2019 Safety of transcranial focused ultrasound stimulation: a systematic review of the state of knowledge from both human and animal studies *Brain Stimul.* **12** 1367–80

Pichardo S, Sin V W and Hynynen K 2011 Multi-frequency characterization of the speed of sound and attenuation coefficient for longitudinal transmission of freshly excised human skulls *Phys. Med. Biol.* **56** 219–50

Pinton G, Aubry J F, Bossy E, Muller M, Pernot M and Tanter M 2012 Attenuation, scattering, and absorption of ultrasound in the skull bone *Med. Phys.* **39** 299–307

Robertson J, Martin E, Cox B and Treeby B E 2017 Sensitivity of simulated transcranial ultrasound fields to acoustic medium property maps *Phys. Med. Biol.* **62** 2559–80

Schneider U, Pedroni E and Lomax A 1996 The calibration of CT Hounsfield units for radiotherapy treatment planning *Phys. Med. Biol.* **41** 111–24

Strohman A, Payne B, In A, Stebbins K and Legon W 2024 Low-intensity focused ultrasound to the human dorsal anterior cingulate attenuates acute pain perception and autonomic responses *J. Neurosci.* **44** e1011232023

Treeby B E and Cox B T 2010 k-Wave: MATLAB toolbox for the simulation and reconstruction of photoacoustic wave fields *J. Biomed. Opt.* **15** 021314

Tsai K W K, Chen J C, Lai H C, Chang W C, Taira T, Chang J W and Wei C-Y 2021 The distribution of skull score and skull density ratio in tremor patients for MR-guided focused ultrasound thalamotomy *Front. Neurosci.* **15** 612940

White D N, Curry G R and Stevenson R J 1978 *The Acoustic Characteristics of the Skull** vol 4 (Pergamon)

White P J, Clement G T and Hynynen K 2006a Longitudinal and shear mode ultrasound propagation in human skull bone *Ultrasound Med. Biol.* **32** 1085–96

White P J, Clement G T and Hynynen K 2006b Local frequency dependence in transcranial ultrasound transmission *Phys. Med. Biol.* **51** 2293–305

Yaakub S N, White T A, Roberts J, Martin E, Verhagen L, Stagg C J, Hall S and Fouragnan E F 2023 Transcranial focused ultrasound-mediated neurochemical and functional connectivity changes in deep cortical regions in humans *Nat. Commun.* **14** 5318

Yoo S, Mittelstein D R, Hurt R C, Lacroix J and Shapiro M G 2022 Focused ultrasound excites cortical neurons via mechanosensitive calcium accumulation and ion channel amplification *Nat. Commun.* **13** 493

Zhang T, Pan N, Wang Y, Liu C and Hu S 2021 Transcranial focused ultrasound neuromodulation: a review of the excitatory and inhibitory effects on brain activity in human and animals *Front. Hum. Neurosci.* **15** 749162